PHYSICAL REVIEW MATERIALS **1**, 024403 (2017)

Tuning the magnetism of epitaxial cobalt oxide thin films by electron beam irradiation

Q. Q. Lan,[1,2] X. J. Zhang,[1,3] X. Shen,[1] H. W. Yang,[1] H. R. Zhang,[1,3] X. X. Guan,[1,3] W. Wang,[1,3] Y. Yao,[1] Y. G. Wang,[1] Y. Peng,[2] B. G. Liu,[1,3,*] J. R. Sun,[1,3,*] and R. C. Yu[1,3,*]

[1]*Beijing National Laboratory for Condensed Matter Physics, Institute of Physics, Chinese Academy of Sciences, Beijing 100190, China*

[2]*Key Laboratory for Magnetism and Magnetic Materials of the Ministry of Education, Lanzhou University, Lanzhou 730000, China*

[3]*School of Physical Sciences, University of Chinese Academy of Sciences, Beijing 100049, China*

(Received 24 March 2017; published 5 July 2017)

Tuning magnetic properties of perovskite thin films is a central topic of recent studies because of its fundamental significance. In this work, we demonstrated the modification of the magnetism of $La_{0.9}Ca_{0.1}CoO_3$ (LCCO) thin films by introducing a stripelike superstructure in a controllable manner using electron beam irradiation (EBI) in a transmission electron microscope. The microstructure, electronic structure, strain change, and origin of magnetism of the LCCO thin films were studied in detail using aberration-corrected scanning transmission electron microscopy, electron energy loss spectroscopy, and *ab initio* calculations based on density functional theory. The results indicate that the EBI-induced unit cell volume expansion accompanies the formation of oxygen vacancies and leads to the spin state transition of Co ions. The low spin state of Co^{4+} ions depress the stripelike superstructure, while higher spin states of Co ions with lower valences are conductive to the formation of "dark stripes". Our work clarifies the origin of magnetism of epitaxial LCCO thin films, benefiting a comprehensive understanding of correlated physics in cobalt oxide thin films.

DOI: 10.1103/PhysRevMaterials.1.024403

I. INTRODUCTION

The magnetism manipulation of $La_{1-x}A_xCoO_3$ (A = Ba, Sr, Ca) thin films with a perovskite structure is at the core of exploring and developing cutting-edge data processing and storage to energy conversion [1–3]. The mysterious magnetic properties of cobalt oxides are closely related to their microstructure. The spin state of Co^{3+} ions, i.e., the high spin (HS) state ($t_{2g}^4e_g^2$, $S = 2$), intermediate (IS) spin state ($t_{2g}^5e_g^1$, $S = 1$), or low spin (LS) state ($t_{2g}^6e_g^0$, $S = 0$), is susceptible to structural deformation because of the competitive mechanisms of crystal-field splitting and Hund's coupling [4,5]. Great efforts have been devoted to tuning the magnetism of such materials through, for example, changing temperature [6,7], applying lattice strains via atomic layer epitaxy [5,8–12], introducing lower valence ions [3,7,13], and constructing superlattices [14,15]. In the previous works, stripelike superstructures were observed in the atomic-level scanning transmission electron microscopy (STEM) images of $LaCoO_3$ (LCO)/$SrTiO_3$ (STO) thin films, which behave as strong ferromagnetism (FM) in contrast with the nonmagnetism (NM) of the bulk LCO [8,16–18]. Recently, we found that the combined tensile lattice strain and Sr doping dramatically affects the spin state of Co ions and thus modifies the magnetic properties of $La_{1-x}Sr_xCoO_3$ ($0 \leqslant x \leqslant 0.1$) thin films, resulting in a decrease of magnetization [19]. Dark Co-O layers in the stripelike superstructure show a strong correlation with the saturation magnetization for the epitaxial $La_{1-x}Sr_xCoO_3$ ($0 \leqslant x \leqslant 0.1$) thin films on both STO and $LaAlO_3$ substrates: more dark Co-O layers, and higher saturation magnetization, suggesting the importance of lattice modulation on FM ordering [19,20]. Some researchers believed that tensile strain causes a LS to HS state transition for parts of the Co^{3+} ions, which results in stripe-shaped structural modulation and the accompanied FM ordering [8,16,21]. In contrast, other researchers attributed the stripelike superstructure to oxygen vacancies and believed that a superexchange (SE) -like hybridization between the HS Co^{2+} and LS Co^{3+} ions is responsible for the magnetism [17]. Both scenarios have received support from various experimental and theoretical works, but, to the best of our knowledge, a consensus has not yet been achieved on the nature of the stripelike superstructure, an ordering of oxygen vacancies, or HS state Co^{3+} ions [8,16,17]. As a result, the explanations of the magnetism of cobalt thin films are still controversial. Compared to the small amounts of Sr doping, the magnetization of the Ca-doping series is qualitatively different for bulk LCO [3,22]. Thus, it is necessary to study the combined lattice strain and Ca-doping effects on the magnetism and microstructure of $La_{1-x}Ca_xCoO_3$ ($0 \leqslant x \leqslant 0.1$) thin films, especially the evolution of dark Co-O layers.

Moreover, recent studies have given clear evidence that the effective magnetic moment of LCO powders, $La_{0.7}Sr_{0.3}CoO_3$ powders, and $La_{0.67}Ca_{0.33}MnO_3$ crystals increases with increasing dosage of electron beam irradiation (EBI), which means that EBI provides another feasible method for the modification of the magnetism of such materials [23–25]. As reported, the EBI usually causes an expansion in unit cell volume, and thus an oxygen vacancy diffusion or a Co-O bond length increases. This in turn leads to a spin state transition of the Co ions, resulting in enhancement of the magnetization of the LCO powders [25]. However, it is still not clear that whether this expansion is evenly shared in unit cells or in an inhomogeneous way by forming superstructures. Meanwhile, the EBI-induced ordering of the oxygen-deficient structure in $La_{2/3}Sr_{1/3}MnO_3$ thin film [26] and in epitaxial LCO/STO superlattices [27] were realized *in situ* transmission electron microscopy (TEM), but its effect on the magnetic properties has not been reported. It suggests that the magnetic properties of cobalt oxide thin films could be tailored by controlling

*Corresponding authors: rcyu@iphy.ac.cn; bgliu@iphy.ac.cn; jrsun@iphy.ac.cn

dark Co-O layers in the films using EBI *in situ* TEM. The experimental data about the EBI effect on strained cobalt oxide thin films at the nanoscale size are scarce, and the magnetism mechanisms are still ambiguous.

In this paper, we modify the magnetism of the $La_{0.9}Ca_{0.1}CoO_3$ (LCCO) epitaxial thin films grown on STO by EBI using an electron accelerator and study the microstructures before and after EBI. Then we perform the EBI experiments for the LCCO thin films *in situ* TEM, focusing on the evolution of the dark Co-O layers in LCCO/STO thin films with the EBI treatments, particularly the evolution of the lattice structure and electronic structure. *Ab initio* calculations were further used to study both the nature of stripelike superstructure and the origins of the magnetism of LCCO/STO thin films before and after EBI treatment. A combination of experimental and theoretical research indicates that the magnetism can be tuned by the EBI *in situ* STEM and that both Ca doping and EBI treatment with the help of lattice strain can control the stripelike superstructure, which is closely related to the magnetism of cobalt oxide thin films.

II. EXPERIMENTAL SECTION

Epitaxial LCCO thin films were grown on (001)-orientated STO substrates (tensile strain $\varepsilon = 2.0\%$), using the pulsed laser ablation technique. Film thickness was about 35 nm and 70 nm, determined by deposition time. Details of sample synthesis can be found elsewhere [19]. The samples for STEM were prepared by mechanical thinning followed by an Ar ion milling in the temperature of liquid nitrogen and cut by focused ion beam with $\pm 2^\circ$ refinement to guarantee the uniform thickness.

The LCCO thin films with the thicknesses of 35 and 70 nm were irradiated with an electron beam using a 0.5 MeV accelerator (AB-0.5). The irradiation was performed at room temperature for 6 kGy, and the beam energy was 0.5 MeV. During the irradiation the entire energy was deposited over the total area of the sample. Magnetic measurements were conducted on a superconducting quantum interface device (VSM-SQUID) magnetometer.

High-resolution aberration-corrected STEM and EELS studies were carried out on a JEOL-ARM200F microscope with double Cs correctors for the condenser lens and objective lens. The available point resolution is better than 0.8 nm at an operating voltage of 200 kV. The spot size is chosen to be 6C for 70-nm-thick and 4C for 35-nm-thick LCCO thin films in the EBI experiments, and a smaller spot size corresponds to a larger probe current. The image recording conditions are a pixel dwell time of 18.9 μs/pixel and pixel size of 0.25 nm^2, and the searching conditions are a pixel dwell time of 2 μs/pixel and pixel size of 4 nm^2 for both 70 and 35 nm LCCO thin films. The high angle annular dark-field (HAADF) images were acquired at an acceptance angles of 90–370 mrad. The energy resolution was measured to be as 0.25 eV at 200 keV.

The atomic positions in the STEM images were measured at subpixel resolution using Peak Pair Analysis software. The A-A interatomic spacing was determined from the average over the unit cells of the marked areas in the HAADF-STEM images. The HAADF images were processed using one-dimensional GPA (software plug-in to Gatan's Digital Micrograph). The radius of the Fourier mask was chosen to be about $1/2a_{sub}$ (a_{sub} is the unit cell parameter of the substrate STO). The phase image was tuned to give the best fit with respect to a reference region, which was chosen in a region of the STO away from the interface.

The first-principles calculations were performed using the projector-augmented wave method as implemented in the Vienna Ab initio Simulation Package [28–32]. The plane wave energy cutoff was set to 600 eV. For the exchange-correlation potential we used the generalized gradient approximation (GGA) of Perdew, Burke, and Ernzerhof [33]. The rotationally invariant GGA + U method was employed with $U = 4.0$ and $J = 0.8$ eV for Co 3*d* electrons [10,34]. All calculations were based on $LaCoO_3$ with $3 \times 2 \times 2$ supercell structure. The unit cell parameters are consistent with the experimental values. One La atom is replaced by Ca atom or one O atom is removed means that the impurity concentration is 1/12 or 1/36. The corresponding experimental lattice constants are $a = b = 3.90$ and $c = 3.75$ Å for LCO, $a = b = 3.88$ and $c = 3.78$ Å for LCCO, and $a = b = 3.92$ and $c = 3.81$ Å for $LCCO_x$ with one O atom removed. Atomic positions were relaxed using a Γ-centered $3 \times 3 \times 3$ k-grid until the Hellmann-Feynmann forces on each atom are reduced to less than 0.01 eV/Å. The convergence criterium for the total energy was chosen to be 10^{-5} eV. The electronic structure calculations were performed by using a Γ-centered $6 \times 6 \times 6$ *k* grid.

III. RESULTS AND DISCUSSION

The LCCO thin films with the thicknesses of 35 and 70 nm were deposited by a pulsed laser ablation technique on STO (001) substrates (details can be found elsewhere [19]). The saturation magnetization and the microstructure of the LCCO thin films were studied before and after EBI treatment by electron accelerator as shown in Fig. 1. The results show that the saturation magnetization of the pristine LCCO thin films is measured to be $\sim 0.2\,\mu_B$/Co, which is significantly lower than that of the LCO/STO thin film ($\sim 0.8\,\mu_B$/Co) [19]. Then the pristine LCCO thin films were carefully checked using a low-dose STEM (spot size of 8C) to avoid EBI as much as we could. In contrast to the well-ordered superstructure of the LCO/STO thin film (Fig. S1 [35]), the LCCO thin film shows a uniform perovskite structure without any obvious dark Co-O layers in the initial state before EBI [Fig. 1(a)], indicating that the doping of smaller ionic radius Ca^{2+} ions depresses the formation of dark Co-O layers, which again verifies the previous report that dark Co-O layers can directly reflect the magnetization [20].

Afterwards, the LCCO thin films were irradiated with an electron beam using a 0.5 MeV accelerator at room temperature for 6 kGy to modify the magnetism. The M-H loops reveal a significant increase in magnetization after EBI [Figs. 1(c) and 1(d)], which is consistent with the previous reports on bulk cobalt oxide: the effective magnetic moment increases with the increasing of EBI dosage [23,25]. Figure S2 shows that the Curie temperature for the irradiated sample is nearly the same as that for the initial state within the margin of error [35]. We further examined the lattice structure of the irradiated LCCO thin films using low-dose STEM (spot size of 8C) and found the appearance of local "dark stripes"

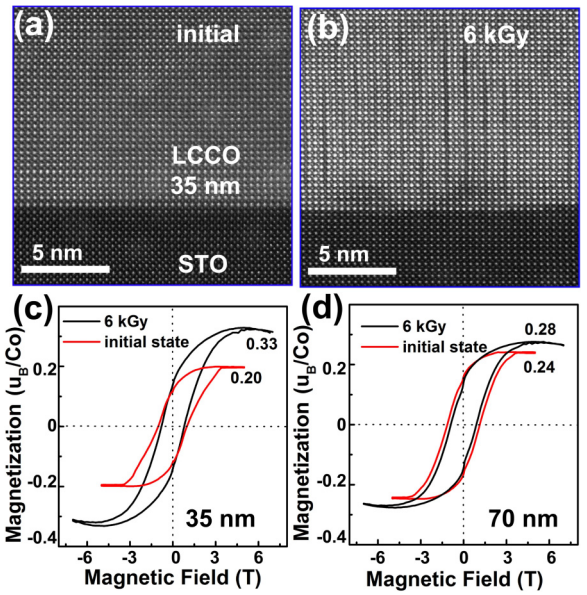

FIG. 1. The HAADF-STEM images of 35-nm-thick LCCO thin films in the initial state (a) and the irradiated state (b) by electron beam with 6 kGy carefully recorded in low-dose STEM (spot size of 8C). The hysteresis curves of the initial (red line) and irradiated with 6 kGy (black line) of the LCCO thin films with the thicknesses of 35 nm (c) and 70 nm (d), measured at 10 K.

as expected [Fig. 1(b)]. These results suggest the potential for modifying the magnetization of LCCO thin films by controlling dark Co-O layers using EBI.

The electron beam in TEM can be used to not only study the microstructure, but also serve as an irradiation source. EBI-induced structural modulation was studied by *in situ* STEM for the LCCO thin films with thicknesses of 70 and 35 nm, respectively. Figure 2 presents the typical STEM HAADF images and the corresponding local fast Fourier transform (FFT) patterns for the 70-nm-thick and 35-nm-thick LCCO thin films, recorded at different stages of the EBI. The 70-nm-thick sample was treated by EBI with a spot size of 6C, a pixel dwell time of 2 μs/pixel, and pixel size of 4 nm^2 in the searching mode. Interestingly, the uniform perovskite structure in the 70-nm-thick film [Fig. 2(a)] was undermined. Dark Co-O layers gradually emerged in some local areas and propagated to the surroundings along the [100] zone axis [Fig. 2(b)], forming the "dark stripes" with a periodicity of $3a_0$ (a_0 is the lattice parameter) perpendicular to the interface. Correspondingly, additional reflections appear as indicated by the red arrows in the FFT pattern [inset in Fig. 2(b)]. With increasing exposure time, dark Co-O layers became denser and denser and steadily grew until the entire irradiation area was covered after 12 min in Fig. 2(c). The final stable stripelike superstructure was generally of $3a_0$ periodicity over the exposure time of 12 min. Meanwhile, a periodicity of $2a_0$ was observed in some local areas as marked by the orange rectangles, the dark Co-O layers parallel to the interface occasional appeared along the [001] zone axis, as indicated by the corresponding reflections in the FFT pattern [the inset in Fig. 2(c), marked by a red arrow]. This result implies that the dark Co-O layers were adjusted to new conditions to release local strains.

To examine the thickness effect on the evolution of "dark stripes" in the epitaxial film, we carried out the EBI

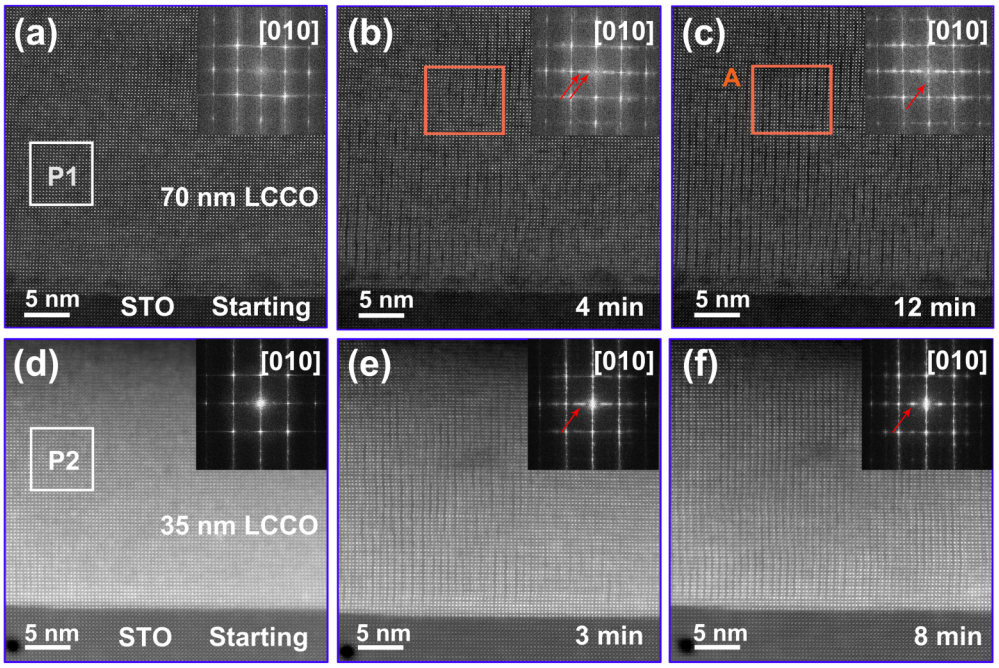

FIG. 2. HAADF-STEM images, demonstrating the structural evolution of the LCCO films during EBI. The images of 70-nm-thick LCCO thin film were recorded at the beginning of irradiation experiment (a) and after irradiation of 4 min (b) and 12 min (c), respectively. The images of 35-nm-thick film were recorded at the beginning of irradiation experiment (d) and after irradiation of 3 min (e) and 8 min (f), respectively. The insets show the corresponding FFT patterns. The red arrows indicate the superstructure reflections. "Dark stripes" gradually emerged and became denser in local areas (marked by the orange rectangles) with increasing exposure time.

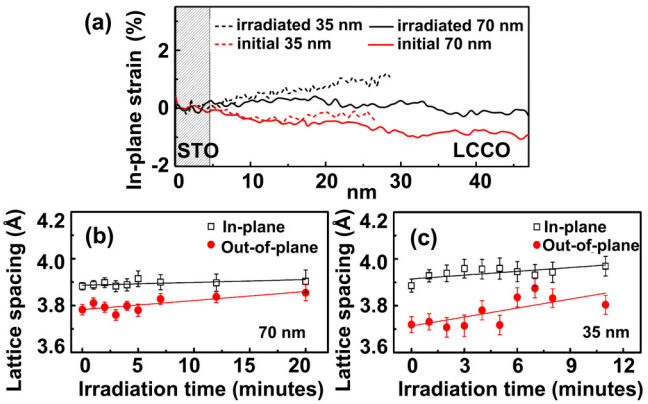

FIG. 3. The in-plane strain profiles as a function of distance d from the substrate to the LCCO thin film of the initial and irradiated areas, determined by averaging data from the white rectangular areas in Fig. S4 [35] (the in-plane strain images of LCCO thin films using GPA method), respectively. The time evolution of lattice spacing at locations P1 (b) extracted from the 70-nm-thick LCCO thin film in Fig. 2(a) and P2 (c) extract from the 35-nm-thick LCCO thin film in Fig. 2(d) during EBI. The in-plane lattice spacings are marked by black squares, and the out-of-plane ones are marked by red dots.

experiments for a 35-nm-thick LCCO/STO film. When this film was exposed to the electron beam the same as that for the 70-nm-thick sample, the film kept the initial state and no dark Co-O layers had been induced by EBI up to an exposure time of 10 min (Fig. S3) [35]. However, when the spot size was reduced to 4C (a smaller spot size corresponds to a larger probe current) while keeping other conditions unchanged, the uniform perovskite structure in the 35-nm-thick film [Fig. 2(d)] was undermined. The dark Co-O layers perpendicular to the interface emerged in 3 min [Fig. 2(e)] and steadily propagated with increasing exposure time until the entire irradiation area was completely transformed to modulated superstructure after about 8 min [Fig. 2(f)]. Notably, the structure experienced a transformation from a mixed periodicity of $2a_0$ and $3a_0$ to a definite $2a_0$ periodicity with increasing exposure time, as illustrated by the additional reflections (marked by the red arrows) in the FFT patterns in the insets of Figs. 2(e) and 2(f). Once formed, as observed in the 70-nm-thick sample, the superstructure was stable under EBI, and no further changes appeared for even longer EBI exposures. These results show that the density of dark Co-O layers and the stripelike superstructure can be tuned in a controllable manner: The larger the current density of electron beam, the darker the Co-O layers and the shorter time it will take to form a stable superstructure.

Moreover, the thinner film (35 nm) needs a larger electron beam current density to reach the final stable state than the thicker one (70 nm) does, because the lattice strain relaxations are different in these two films: In general, the thinner film will be more firmly clamped by substrate, thus in a highly strained state. As a result, a higher energy is required to break the energy barrier between the strained state and the relaxed state. Figure 3(a) presents the in-plane strain ε_{xx} profiles in the LCCO film as a function of distance d from the LCCO/STO interface, extracted from the strain maps of ε_{xx} basing on geometrical phase analysis (GPA) as shown in Fig. S4 [35–38]. The positive value means the parameter is larger than that of STO substrate while the negative value means it is smaller. Before electron irradiation, the ε_{xx} value is negative for the 70-nm-thick film and significantly increases in magnitude as the distance from the interface increases. This is a signature of in-plane lattice relaxation. In contrast, the ε_{xx} for the 35-nm-thick film is close to zero, indicating a nearly fully strained state of this film. This means that the thin film is more firmly clamped by the substrate than the thick one. Interestingly, electron irradiation causes a visible lattice expansion, as indicated by the increase of ε_{xx} with d. This effect is observed for both the thin and thick films, and therefore is a general feature of the irradiation effect. It means an in-plane lattice expansion after the EBI, i.e., the appearance of vertical "dark stripes" enlarge the separation between lattice sites. Figures 3(b) and 3(c) show the in-plane and out-of-plane average lattice spacings as functions of irradiation time, extracted at the locations of P1 and P2 as marked by the white squares in Figs. 2(a) and 2(d), respectively. One can observe that both the in-plane and out-of-plane lattice constants show a continuous increase with irradiation time, indicating an expansion of the unit cell of LCCO. This result is consistent with that of Fig. 3(a). Notably, the lattice parameters of the thinner film (irradiated by larger beam current; spot size is 4C) expand more rapidly than that of the thicker film (spot size is 6C), revealing that the strain can also be tuned by the current density of EBI.

From the discussion above, we may reasonably conclude that since the thinner LCCO film is better strained by the underlying STO substrate than the thicker one, and higher excitation energy from EBI is needed to break the balance of the tensile strain energy and the lattice energy of LCCO. While the LCCO thin film is exposed to the EBI, the lattice structure is rearranged to meet the lowest energy principle, and a stripelike superstructure is thus formed. In general, the clamping from the substrate causes the film to be uniformly strained, while the requirement to reduce elastic energy calls for a lattice relaxation. The EBI breaks the energy barrier between the fully strained and relaxed states, triggering the lattice relaxation. The periodicity of $2a_0$ or $3a_0$ of the stripelike superstructure is a result of the balance of these two competitive mechanisms. Thus, the density of the dark Co-O layers can be controlled by the EBI method.

It is important to mention that the lattice expansion, in general, has the tendency to change the hybridization between Co-O atoms by changing the Co-O bond or Co-O-Co angles, or forming new superstructures. To elucidate the EBI-induced local lattice structure change in more detail, the maps of the in-plane A (La/Ca)-A (La/Ca) interatomic spacings extracted from the HAADF-STEM images of the uniform structures and the $3a_0$ and $2a_0$ period stripelike superstructures of LCCO thin films are presented in Fig. S5 [35]. The results show that the average of in-plane lattice spacing of the LCCO thin film in the initial state is uniform and about 3.88 ± 0.02 Å. But after EBI, the average A-A interatomic spacings across the dark Co-O layers are all larger than that across the bright Co-O layers in the stripelike superstructures: 4.44 ± 0.03 Å across the dark Co-O layers, 3.76 ± 0.02 Å and 3.78 ± 0.03 Å across the bright Co-O layers for the $3a_0$ superstructure; 4.38 ± 0.09 Å across the dark Co-O layers, 3.56 ± 0.09 Å across the bright Co-O layers for the $2a_0$ superstructure. EBI-induced lattice

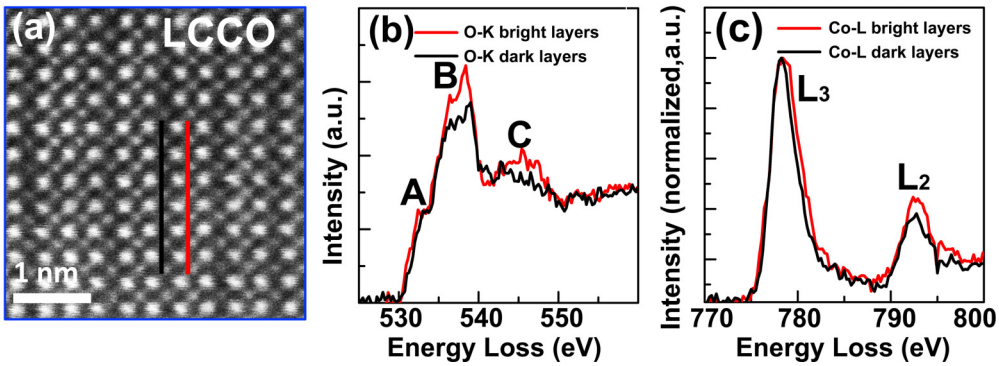

FIG. 4. The EELS fine structures across the stripe patterns of the 35-nm-thick LCCO thin films (a). The black line and red line were obtained from the dark and bright Co-O layers, respectively. (b) O K edges. (c) Co $L_{2,3}$ edges.

expansion was also reported in bulk cobalt oxide perovskites. However, to our best knowledge, neither superstructures nor essential change of unit cell symmetry was detected [7,10]. In bulk cobalt oxide perovskite, the usual thermal expansion accumulated under EBI leads to the recrystallization and corresponding increase of lattice volume [25], which is different from the thin films with substrate strain constraint.

The distortion of the CoO_6 octahedra across the dark Co-O layers can be related to the Jahn-Teller distortion caused by the orbital ordering, which influences the electronic structure of the perovskite by forming oxygen vacancies and/or converting the spin state of Co ions. Figures 4(b) and 4(c) show the O-K edge and Co-L near-edge spectra of the 35-nm-thick film, recorded across the dark and bright Co-O layers in Fig. 4(a). The O-K edge structure in EELS spectra provides the information on the excitations from O 1*s* to 2*p* bands. Three characteristic O-K edge peaks, labeled by A, B and C, are observed in Fig. 4(b), which can be assigned to the hybridization of O 2*p* with Co 3d, La 5*d,* and Co 4*sp,* respectively [39,40]. We can see that the intensity of the peaks in the O-K edge spectrum of the dark Co-O layers is generally weaker than that of the bright Co-O layers [Fig. 4(b)]. Both the intensity of the prepeak A and its energy separation with the adjacent main peak B were found to decrease in the dark Co-O layers compared to the bright layers, indicating a decrease in Co valence in the dark Co-O layers [41,42]. The ratio of Co L_3/L_2 is about 4.89 ± 0.12 for the dark Co-O layers and 3.74 ± 0.21 for the bright Co-O layers [Fig. 4(c)], confirming the decrease of Co valence in dark Co-O layers [43]. This is a lateral evidence that the content of O vacancies is higher in the dark Co-O layers. Similar phenomena are also observed for the 70-nm-thick LCCO thin film as shown in Fig. S6 [35].

The spin-state ordering associated with the atomic-spacing modulation was studied and confirmed using *ab initio* calculations. We started our calculations by searching for the most stable magnetic solutions, which are well matched with the experimental magnetization and microstructure. We first validate our approach against known properties of the LCO thin films as a comparison as shown in Fig. S7 [35]. The results show that the FM order is established via the pseudo-SE interaction between HS Co^{3+} and LS Co^{3+} atoms with magnetic moments of 2.95 and $0.30\,\mu_B$ at the dark Co-O layers, as described by the Goodenough-Kanamori rule [21,28,29,44]. The calculated average magnetic moment of LCO is $0.65\,\mu_B$/Co, which is close to the experimental one of $0.8\,\mu_B$/Co.

When the larger radius La^{3+} ions are partially substituted by the smaller radius Ca^{2+} ions, the LCCO thin films show a uniform perovskite structure without any obvious dark Co-O layers and a magnetization of $\sim 0.2\,\mu_B$/Co in the initial state before EBI. Based on the above experimental results, different assumptive structures with zero magnetic moment were calculated. Figure 5(a) presents the final optimized structure and magnetization of LCCO. The La-La spacing distances around Ca^{2+} ion at the first and second columns are both 3.86 Å, revealing that Ca^{2+} ions doping in LCO thin films homogenizes the La-La spacing distance around Ca^{2+} ion and decreases the number of dark Co-O layers. Our calculations suggest the LCCO thin films are nonmagnetic, which is well matched with the experimental value of $\sim 0.2\,\mu_B$/Co. The weak residual magnetization may come from the inhomogeneous Ca doping. The density of states (DOS) result in Fig. 5(b) shows that the HS state Co ions transform to LS state, and a few hole carriers are introduced after Ca doping. It can be concluded that the substitution of smaller radius Ca^{2+} ions for larger radius La^{3+} ions will cause a transformation from HS Co^{3+} to LS Co^{4+} ions on the combined effect of the strain-induced structural change and Ca^{2+} doping-induced chemical change [3,13,45]. The LS

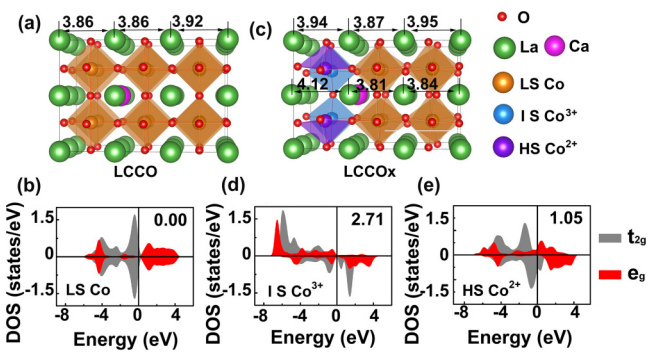

FIG. 5. The optimized structures and magnetization of LCCO (a) and LCCO with O vacancies (c). Orange, cyan, and purple ions represent LS Co ions, IS Co^{3+} ions, and HS Co^{2+} ions, respectively. Red, blue, and magenta ions represent O, La, and Ca ions. The DOS of Co atoms of LCCO (b) and LCCO with O vacancies (d, e) at the corresponding positions given in (a) and (c).

TABLE I. Occupation of the Co d orbitals in LCO and $LCCO_x$; the positions of Co ions are given in Fig. 5 and Fig. S7 [35].

System	LCO				$LCCO_x$			
Magnetic moment of Co	2.95 (HS Co^{3+})				2.71(HS Co^{2+})			
Orbital	$t_{2g}^{\uparrow}$	$t_{2g}^{\downarrow}$	$e_g^{\uparrow}$	$e_g^{\downarrow}$	$t_{2g}^{\uparrow}$	$t_{2g}^{\downarrow}$	$e_g^{\uparrow}$	$e_g^{\downarrow}$
Occupation	2.94	1.42	2.03	0.63	2.92	1.40	1.96	0.80
Magnetic moment of Co	0.30 (LS Co^{3+})				1.05 (IS Co^{3+})			
Orbital	$t_{2g}^{\uparrow}$	$t_{2g}^{\downarrow}$	$e_g^{\uparrow}$	$e_g^{\downarrow}$	$t_{2g}^{\uparrow}$	$t_{2g}^{\downarrow}$	$e_g^{\uparrow}$	$e_g^{\downarrow}$
Occupation	2.92	2.85	0.87	0.66	2.90	2.51	1.22	0.57

Co^{4+} ions suppress the ordering arrangement of HS Co^{3+} ions thus cause the vanishing of dark Co-O layers. Since the number of HS Co^{3+} ions decreases, the pseudo-SE between HS-LS-HS Co^{3+} ions which gives rise to the FM order of the LCO/STO film is weakened [8,20].

While the LCCO thin film is exposed to EBI, the unit cell volume of LCCO thin film expands and the superstructure with dark Co-O layers gradually forms. Salawu *et al.* [33] reported that modifying the chemical composition of LCO by doping with divalent Ca ions for trivalent La ions lowers the O vacancy formation energy, indicating that the O vacancies easily form in the stimulation. The EELS result in Fig. 4 also shows that there are oxygen vacancies in the dark Co-O layers, so we calculated the LCCO with O vacancies ($LCCO_x$) in Fig. 5(c). Elongated La-La interatomic spacing reemerges, and the two kinds of Co ions with magnetic moment of 2.71 (purple) and 1.05 μ_B (cyan) reappear neighboring the O vacancies. The occupation of Co d orbitals is evidenced by the DOS in Figs. 5(d) and 5(e). The detailed occupation is given in Table I. The occupation of $e_g^{\downarrow}$ orbital for the Co (2.71 μ_B) ions neighboring an O vacancy in $LCCO_x$ is higher than that for the Co (2.95 μ_B) ions in LCO, while the occupations of $t_{2g}^{\downarrow}$, $t_{2g}^{\uparrow}$, and $e_g^{\uparrow}$ are close to each other within the margin of error. This indicates that the valence state of HS state Co ions (2.71 μ_B) in $LCCO_x$ decreases to Co^{2+} compared to the HS Co^{3+} (2.95 μ_B) in LCO. The electrons in $t_{2g}^{\downarrow}$ orbital transfer to the $e_g^{\uparrow}$ orbital of the Co ions (1.05 μ_B) of $LCCO_x$, compared to the LS Co^{3+} (0.30 μ_B) in LCO. In consideration of the electric neutrality, the Co ions with the moment of 1.05 μ_B prefer to be in the IS state of Co^{3+}. The calculated magnetic moment of $LCCO_x$ after EBI treatment is 0.63 μ_B/Co, which is obviously larger than that of LCCO thin film without any obvious dark Co-O layers. In this case, we consider that the double-exchange (DE) interaction between HS Co^{2+} ions and IS Co^{3+} ions is responsible for the FM magnetism of the EBI treated LCCO thin film. The EBI-induced oxygen vacancies are conductive to the ordering of higher spin state Co ions with lower valences and the formation of dark Co-O layers. Our calculation provides another theoretical evidence for the experimental results that the effective magnetic moment increases with increasing EBI dosage in such materials [13,23].

IV. CONCLUSIONS

We have demonstrated a magnetization tuning way of controlling the formation and evolution of dark Co-O layers in the LCCO thin films in the exposing of electron beam *in situ* STEM. The EBI on the film leads to an expansion of the unit cell volume, thereby gradually causing a stripelike superstructure, which is constrained by the electron beam current density, strain energy from the substrate, and crystal energy of the film. The theoretical calculations indicate that the smaller radius Ca^{2+} doping in LCO thin films transforms the HS Co^{3+} ions in the dark Co-O layers to LS Co ions and decreases the number of magnetic Co ions and the pseudo-SE interaction between HS-LS-HS Co^{3+} ions. While the LCCO thin film is exposed to EBI, oxygen vacancies exist in the dark Co-O layers and are conductive to transforming LS Co ions to HS Co^{2+} and IS Co^{3+}, and the DE interaction between HS Co^{2+} and IS Co^{3+} in the dark Co-O layers increases. It can be concluded that the LS Co^{4+} ions depress the stripelike superstructure, while higher spin states of Co ions with low valences are conductive to the formation of "dark stripes" in cobalt oxide thin films. Our results pave the way for not only tuning the magnetization of the LCCO thin film artificially by EBI, but also a deeper understanding of the origins of magnetism of LCCO thin films, which is of great significance for the designing of the future devices using LCCO-related materials.

ACKNOWLEDGMENTS

R.C.Y., B.G.L., and J.R.S. designed and arranged the experiments and calculations. H.W.Y. and H.R.Z. fabricated the LCCO thin films. Q.Q.L. fabricated the STEM samples. X.S. and Q.Q.L. carried out the STEM and EELS experiments. Q.Q.L., X.S., and R.C.Y. performed data analyses. X.J.Z. and B.G.L. performed the theoretical calculations. Q.Q.L. and R.C.Y. wrote the manuscript. Y.Y., Y.G.W., Y.P., B.G.L., and J.R.S. revised the manuscript. All authors discussed the results and commented on the manuscript. This work was supported by the National Key Research Program of China (Grant No. 2016YFA0300701) and the National Natural Science Foundation of China (Grants No. 11574376 and No. 11374343).

Q.Q.L. and X.J.Z. contributed equally to this work.

[1] J. H. Lee, L. Fang, E. Vlahos, X. Ke, Y. W. Jung, L. F. Kourkoutis, J. W. Kim, P. J. Ryan, T. Heeg, M. Roeckerath, V. Goian, M. Bernhagen, R. Uecker, P. C. Hammel, K. M. Rabe, S. Kamba, J. Schubert, J. W. Freeland, D. A. Muller, C. J. Fennie,

P. Schiffer, V. Gopalan, E. Johnston-Halperin, and D. G. Schlom, Nature (London) **466**, 954 (2010).
[2] C. Song, S. Havlin, and H. A. Makse, Nature (London) **433**, 392 (2005).
[3] M. Kriener, M. Braden, H. Kierspel, D. Senff, O. Zabara, C. Zobel, and T. Lorenz, Phys. Rev. B **79**, 224104 (2009).
[4] A. Ishikawa, J. Nohara, and S. Sugai, Phys. Rev. Lett. **93**, 136401 (2004).
[5] J. Fujioka, Y. Yamasaki, H. Nakao, R. Kumai, Y. Murakami, M. Nakamura, M. Kawasaki, and Y. Tokura, Phys. Rev. Lett. **111**, 027206 (2013).
[6] D. Phelan, D. Louca, K. Kamazawa, S.-H. Lee, S. N. Ancona, S. Rosenkranz, Y. Motome, M. F. Hundley, J. F. Mitchell, and Y. Moritomo, Phys. Rev. Lett. **97**, 235501 (2006).
[7] M. Merz, D. Fuchs, A. Assmann, S. Uebe, H. v. Löhneysen, P. Nagel, and S. Schuppler, Phys. Rev. B **84**, 014436 (2011).
[8] W. S. Choi, J. H. Kwon, H. Jeen, J. E. Hamann-Borrero, A. Radi, S. Macke, R. Sutarto, F. He, G. A. Sawatzky, V. Hinkov, M. Kim, and H. N. Lee, Nano Lett. **12**, 4966 (2012).
[9] D. Fuchs, E. Arac, C. Pinta, S. Schuppler, R. Schneider, and H. v. Löhneysen, Phys. Rev. B **77**, 014434 (2008).
[10] R. F. Klie, T. Yuan, M. Tanase, G. Yang, and Q. Ramasse, Appl. Phys. Lett. **96**, 082510 (2010).
[11] R. Aso, D. Kan, Y. Shimakawa, and H. Kurata, Adv. Funct. Mater. **24**, 5177 (2014).
[12] D. Kan, R. Aso, H. Kurata, and Y. Shimakawa, Adv. Funct. Mater. **23**, 1129 (2013).
[13] D. Zhang, X. Mi, Q. Wu, X. Zhang, and G. Tang, Solid State Commun. **201**, 49 (2015).
[14] P. Gao, J. Britson, C. T. Nelson, J. R. Jokisaari, C. Duan, M. Trassin, S. H. Baek, H. Guo, L. Li, Y. Wang, Y. H. Chu, A. M. Minor, C. B. Eom, R. Ramesh, L. Q. Chen, and X. Pan, Nat. Commun. **5**, 3801 (2014).
[15] L. Qiao, J. H. Jang, D. J. Singh, Z. Gai, H. Xiao, A. Mehta, R. K. Vasudevan, A. Tselev, Z. Feng, H. Zhou, S. Li, W. Prellier, X. Zu, Z. Liu, A. Borisevich, A. P. Baddorf, and M. D. Biegalski, Nano Lett. **15**, 4677 (2015).
[16] J.-H. Kwon, W. S. Choi, Y.-K. Kwon, R. Jung, J.-M. Zuo, H. N. Lee, and M. Kim, Chem. Mater. **26**, 2496 (2014).
[17] N. Biškup, J. Salafranca, V. Mehta, M. P. Oxley, Y. Suzuki, S. J. Pennycook, S. T. Pantelides, and M. Varela, Phys. Rev. Lett. **112**, 087202 (2014).
[18] V. V. Mehta, N. Biskup, C. Jenkins, E. Arenholz, M. Varela, and Y. Suzuki, Phys. Rev. B **91**, 144418 (2015).
[19] H. W. Yang, H. R. Zhang, Y. Li, S. F. Wang, X. Shen, Q. Q. Lan, S. Meng, R. C. Yu, B. G. Shen, and J. R. Sun, Sci. Rep. **4**, 6206 (2014).
[20] Q. Q. Lan, X. Shen, H. W. Yang, H. R. Zhang, J. Zhang, X. X. Guan, Y. Yao, Y. G. Wang, R. C. Yu, Y. Peng, and J. R. Sun, Appl. Phys. Lett. **107**, 242404 (2015).
[21] H. Seo, A. Posadas, and A. A. Demkov, Phys. Rev. B **86**, 014430 (2012).
[22] M. Kriener, C. Zobel, A. Reichl, J. Baier, M. Cwik, K. Berggold, H. Kierspel, O. Zabara, A. Freimuth, and T. Lorenz, Phys. Rev. B **69**, 094417 (2004).
[23] C. J. Benedict, A. Rao, G. Sanjeev, G. S. Okram, and P. D. Babu, J. Magn. Magn. Mater. **397**, 145 (2016).
[24] T. I. Arbuzova and S. V. Naumov, Phys. Solid State **55**, 64 (2013).
[25] V. V. Efimov, E. A. Efimova, K. Iakoubovskii, D. V. Karpinskii, S. Khasanov, D. I. Kochubey, V. V. Kriventsov, A. Kuzmin, A. P. Sazonov, V. Sikolenko, M. Sakharov, A. N. Shmakov, and S. I. Tiutiunnikov, J. Phys. Chem. Solids **67**, 2001 (2006).
[26] L. Yao, S. Majumdar, L. Akaslompolo, S. Inkinen, Q. H. Qin, and S. van Dijken, Adv. Mater. **26**, 2789 (2014).
[27] J. Hyuck Jang, Y.-M. Kim, Q. He, R. Mishra, L. Qiao, M. D. Biegalski, A. R. Lupini, S. T. Pantelides, S. J. Pennycook, S. V. Kalinin, and A. Y. Borisevich, Microsc. Microanal. **20**, 422 (2014).
[28] J. B. Goodenough, Struct. Bonding (Berlin) **98**, 1 (2001).
[29] F. Cossu, N. Singh, and U. Schwingenschlögl, Appl. Phys. Lett. **102**, 042401 (2013).
[30] G. Kresse and D. Joubert, Phys. Rev. B **59**, 1758 (1999).
[31] P. E. Blöchl, Phys. Rev. B **50**, 17953 (1994).
[32] K. Knížek, Z. Jirák, J. Hejtmánek, P. Novák, and W. Ku, Phys. Rev. B **79**, 014430 (2009).
[33] A. S. Omotayo, G. Li-Yong, and S. Udo, Europhys. Lett. **114**, 26001 (2016).
[34] J. Gazquez, W. Luo, M. P. Oxley, M. Prange, M. A. Torija, M. Sharma, C. Leighton, S. T. Pantelides, S. J. Pennycook, and M. Varela, Nano Lett. **11**, 973 (2011).
[35] See Supplemental Material at http://link.aps.org/supplemental/10.1103/PhysRevMaterials.1.024403 for more images and supporting discussion.
[36] S. Turner, O. I. Lebedev, J. Verbeeck, K. Gehrke, V. Moshnyaga, and G. Van Tendeloo, Phys. Rev. B **87**, 035418 (2013).
[37] C. Dubourdieu, J. Bruley, T. M. Arruda, A. Posadas, J. Jordan-Sweet, M. M. Frank, E. Cartier, D. J. Frank, S. V. Kalinin, A. A. Demkov, and V. Narayanan, Nat. Nano. **8**, 748 (2013).
[38] H. B. Kim, G. Hobler, A. Steiger, A. Lugstein, and E. Bertagnolli, Nanotechnology **18**, 265307 (2007).
[39] J. M. Vila-Fungueiriño, B. Rivas-Murias, B. Rodríguez-González, and F. Rivadulla, Chem. Mater. **26**, 1480 (2014).
[40] R. F. Klie, J. C. Zheng, Y. Zhu, M. Varela, J. Wu, and C. Leighton, Phys. Rev. Lett. **99**, 047203 (2007).
[41] W. Luo, M. Varela, J. Tao, S. J. Pennycook, and S. T. Pantelides, Phys. Rev. B **79**, 052405 (2009).
[42] M. Varela, M. P. Oxley, W. Luo, J. Tao, M. Watanabe, A. R. Lupini, S. T. Pantelides, and S. J. Pennycook, Phys. Rev. B **79**, 085117 (2009).
[43] Z. L. Wang, J. S. Yin, and Y. D. Jiang, Micron **31**, 571 (2000).
[44] H. Hsu, P. Blaha, and R. M. Wentzcovitch, Phys. Rev. B **85**, 140404 (2012).
[45] X. L. Wang and E. Takayama-Muromachi, Phys. Rev. B **72**, 064401 (2005).